High-resolution, high-contrast mid-infrared imaging of fresh biological samples with ultraviolet-localized photoacoustic microscopy

Junhui Shi [1], Terence T. W. Wong[1,2,3], Yun He[1,2], Lei Li[1], Ruiying Zhang[2], Christopher S. Yung [4], Jeeseong Hwang[4], Konstantin Maslov[1] and Lihong V. Wang [1]*

Mid-infrared (MIR) microscopy provides rich chemical and structural information about biological samples, without staining. Conventionally, the long MIR wavelength severely limits the lateral resolution owing to optical diffraction; moreover, the strong MIR absorption of water ubiquitous in fresh biological samples results in high background and low contrast. To overcome these limitations, we propose a method that employs photoacoustic detection highly localized with a pulsed ultraviolet laser on the basis of the Grüneisen relaxation effect. For cultured cells, our method achieves water-background suppressed MIR imaging of lipids and proteins at ultraviolet resolution, at least an order of magnitude finer than the MIR diffraction limits. Label-free histology using this method is also demonstrated in thick brain slices. Our approach provides convenient high-resolution and high-contrast MIR imaging, which can benefit the diagnosis of fresh biological samples.

As a vibrational imaging modality, MIR microscopy has been exploited for applications ranging from material characterization[1–3] to label-free histologic analysis[4–7]. In the past two decades, the sensitivity and speed of MIR microscopy have been improved significantly[8–13], but its biomedical applications still face limitations. First, conventional transmission MIR microscopy can image only dried or thin samples[1], which requires complicated and time-consuming preparation[6]. In addition, the lateral resolution is diffraction-limited to approximately the long MIR wavelength at a typically used numerical aperture (~0.5). Furthermore, for fresh biological samples, the broadband and strong MIR absorption of water creates a huge background, compromising imaging contrast and interfering with molecular analysis.

Many techniques have improved MIR microscopy by addressing one or two of the above limitations. Attenuated total reflection–Fourier transform infrared (ATR-FTIR) microspectroscopic imaging[14,15], a now widely used standard technology, can measure fresh samples in reflection mode with improved spatial resolution, but its penetration depth—due to the use of evanescent waves—is limited to only 1–2 μm. Atomic force microscopy (AFM) has achieved nanoscale resolution by detecting thermal expansion[16–18], light scattering[19] or force[20] induced by MIR laser absorption; however, the surface contact or near-field detection poses challenges in scanning fresh biological samples. Photothermal MIR imaging[21–24], which employs a continuous-wave visible or near-IR laser beam to detect the MIR thermal lensing effect, greatly improves the resolution and somewhat reduces the water background, but the scattering-based detection method restricts its applications to only translucent samples. Stimulated Raman scattering (SRS) imaging has demonstrated label-free chemical mapping of biological cells and tissues at high spatial resolution and contrast[25–27]. Also, far-field

super resolution has been achieved using stimulated emission depletion[28,29]. In photoacoustic imaging techniques, although photoacoustic infrared (PAIR) detection was invented decades ago for spectroscopy and sensing of totally opaque or highly light-scattering materials[30–33], it has only recently been demonstrated in imaging of thick and scattering fresh biological samples without thin slicing[34]. However, it does not address the drawbacks in either spatial resolution or the water background.

Here, we present a novel approach, called ultraviolet-localized MIR photoacoustic microscopy (ULM-PAM), to achieve high-resolution and nearly water-background-free MIR imaging of fresh biological samples. In our approach, a pulsed mid-MIR laser thermally excites the sample at a focal spot, and a confocal pulsed ultraviolet laser beam photoacoustically detects the resulting transient temperature rise, thereby reporting the magnitude of the MIR absorption by the sample. This detection scheme is based on the fact that a temperature rise in a sample enhances photoacoustic signals, a phenomenon called the Grüneisen relaxation effect[35,36]. While our imaging method reveals MIR absorption contrast, its lateral resolution is determined by the ultraviolet wavelength, which is one order of magnitude shorter than the MIR wavelength. In addition, ultraviolet light in the range of 200–230 nm is highly absorbed by most biomolecules, such as lipids, proteins and nucleic acids[37–39], but it is totally transmissive in water[40]. Thus, the strong water background of MIR absorption is suppressed in our method. Furthermore, the ultraviolet light can penetrate up to 100 μm (ref. [41]), greater than MIR penetration in fresh specimens[23], and the photoacoustic signal can propagate in biological tissues with negligible scattering. Therefore, ULM-PAM enables high-resolution and water-background-suppressed photoacoustic MIR imaging of fresh thick and scattering biological samples.

[1]Caltech Optical Imaging Laboratory, Andrew and Peggy Cherng Department of Medical Engineering, Department of Electrical Engineering, California Institute of Technology, Pasadena, CA, USA. [2]Optical Imaging Laboratory, Department of Biomedical Engineering, Washington University in St Louis, St Louis, MO, USA. [3]Present address: Translational and Advanced Bioimaging Laboratory, Department of Chemical and Biological Engineering, Hong Kong University of Science and Technology, Hong Kong, China. [4]Applied Physics Division, National Institute of Standards and Technology, Boulder, CO, USA. *e-mail: LVW@caltech.edu

Results

Photoacoustic generation depends on the optical absorption coefficient as well as the pre-laser-pulse temperature. When an object absorbs a short laser pulse, thermal expansion causes it to emit a photoacoustic signal. The amplitude of the photoacoustic signal is proportional to the absorbed optical energy density, with a coefficient called the Grüneisen parameter (Γ). Γ depends on the volume expansion coefficient and the speed of sound, both of which are temperature-dependent and quasi-linearly proportional to the pre-pulse temperature. As a result, in the physiological temperature range, the Grüneisen parameter depends linearly on the pre-pulse temperature (T), and $\Delta\Gamma/\Gamma \approx 0.04\Delta T$ around $20\,^\circ\mathrm{C}$ for water-rich soft biological tissues[42,43], where Δ denotes a small change. Therefore, a pre-pulse temperature rise of $1\,^\circ\mathrm{C}$ can enhance the photoacoustic signal by ~4%, and this relationship has been used to photoacoustically measure temperature in tissues[44–46]. When a pulsed laser induces a local transient temperature rise, the local Grüneisen parameter increases within the thermal confinement time (that is, the time before the local heat diffuses away), which is termed the Grüneisen relaxation effect[35,36]. On this basis, ULM-PAM uses a pulsed ultraviolet laser to photoacoustically measure the temperature rise induced by absorption of pulsed MIR laser illumination by the sample.

We realize ULM-PAM using a two-step measurement scheme, as illustrated in Fig. 1a. First, an ultraviolet laser pulse generates a baseline photoacoustic signal (PA_{UV1}), which is used in conventional ultraviolet photoacoustic microscopy (UV-PAM)[41,47]. Second, we use dual sequential pulses for MIR heating and ultraviolet probing. As soon as an MIR laser pulse heats up the same region, a second ultraviolet laser pulse induces another photoacoustic signal (PA_{UV2}), where the two laser pulses are separated by a sub-microsecond time interval (Δt) that is shorter than the thermal confinement time. In water-rich soft biological tissues, biological molecules are distributed sparsely in the water environment, and the specific heat capacity is approximately homogenous; therefore, the local temperature rise (ΔT) induced by the MIR laser pulse is approximately proportional to the MIR absorption coefficient. Because the local temperature rise increases the local Grüneisen parameter, PA_{UV2} is stronger than PA_{UV1}. The fractional change in photoacoustic amplitude, %ΔPA (defined as $\Delta PA/PA_{UV1}$, where $\Delta PA = PA_{UV2} - PA_{UV1}$), is proportional to ΔT, which is proportional to the absorption coefficient at the MIR wavelength. Because the ultraviolet wavelength is at least one order of magnitude shorter than the MIR wavelength, the spatial resolution is mainly determined by the focal diameter of the ultraviolet laser beam (Fig. 1b). Consequently, the lateral resolution is diffraction limited to $\lambda_{UV}/2NA$, where λ_{UV} is the ultraviolet wavelength, and NA is the numerical aperture of the objective lens. Because the highest practical NA is approximately 0.5 for both MIR and ultraviolet imaging, our approach improves the MIR imaging resolution by at least one order of magnitude from approximately the MIR wavelength to the ultraviolet wavelength. In addition, as water has an extremely low absorption coefficient ($<0.3\,\mathrm{m}^{-1}$) in the ultraviolet region of 200–230 nm (Supplementary Fig. 1), the water background from MIR absorption in fresh biological samples is suppressed.

The experimental set-up of ULM-PAM is shown in Fig. 1c. The system consists of a pulsed optical parametric oscillator (OPO) MIR (2.5–12.0 μm, 10 ns pulse duration) laser and a pulsed OPO ultraviolet laser (210–280 nm, 10 ns pulse duration). The two laser beams are combined by a germanium dichroic mirror and then delivered through an aluminium-coated reflective objective lens (NA = 0.52) to a transmission-mode photoacoustic microscopy system. Both the ultraviolet and MIR laser beams are focused on the sample, which is mounted on a CaF₂ window attached to the bottom of a water tank. The focal sizes of the ultraviolet and MIR are nearly diffraction-limited. Configured in transmission mode, an ultrasonic transducer
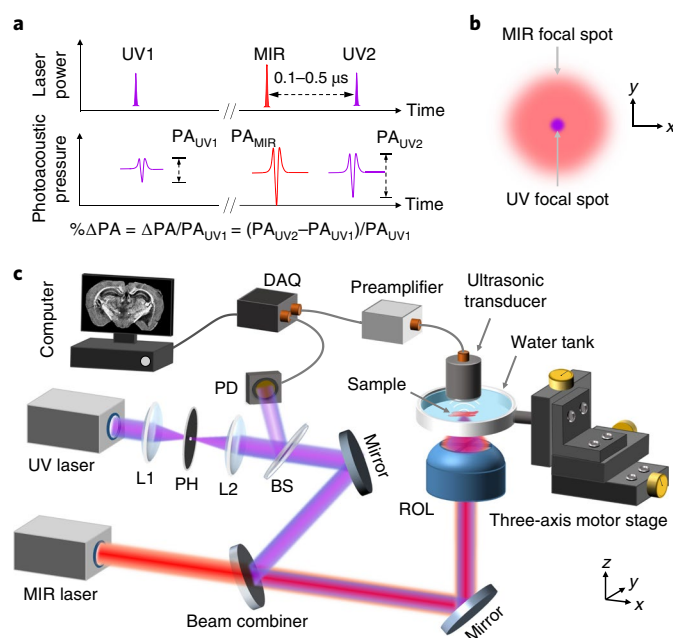
Fig. 1 | Ultraviolet-localized MIR photoacoustic microscopy (ULM-PAM). a, Principle of ULM-PAM. Two ultraviolet laser pulses generate photoacoustic signals PA_{UV2} and PA_{UV1} before and after MIR laser excitation. Because the MIR absorption increases the Grüneisen parameter, PA_{UV2} is greater than PA_{UV1}; thus, %ΔPA reveals the MIR absorption. **b**, Confocal illumination areas of the MIR and ultraviolet laser beams on the focal plane. **c**, Schematic of the experimental set-up. The ultraviolet and MIR laser beams are confocally delivered to the sample in a transmission-mode photoacoustic microscope. BS, beamsplitter; DAQ, data acquisition unit; L1, L2, lenses; PD, photodiode; PH, pinhole; ROL, reflective objective lens consisting of a convex followed by a concave mirror (details not shown). The electronic connections for controls are not shown. The data acquisition speed is limited by the pulse repetition rate of the MIR laser, which is 1 kHz.

(25 MHz centre frequency) is confocally aligned with the MIR and ultraviolet optical foci and collects the photoacoustic signals generated by the ultraviolet or MIR lasers. The output energy of the ultraviolet laser is monitored by a photodiode for pulse-to-pulse calibration of the pulse energy. The time delay between the MIR and ultrviolet laser pulses is controlled by a delay generator and set around 100–500 ns, which is within the thermal confinement time for hydrated biological samples. The data acquisition, stage scanning and laser wavelength adjustment are all controlled by a computer. Because the current MIR laser has a pulse repetition rate of up to only 1 kHz, we implement the two-step measurement scheme with two line scans along the x axis instead of one point per step. In two consecutive line scans along the same line, PA_{UV1} with the MIR laser off then PA_{UV2} with the laser on are acquired. In practice, we repeat this two-step scan for each line to improve the signal-to-noise ratio. Once the line scans along each x axis are completed, the sample is stepwise translated along the y axis to form a two-dimensional (2D) image.

To characterize our technology using non-biological samples, we first illustrate the ULM-PAM imaging procedure using a 6-μm-diameter carbon fibre on a CaF₂ substrate. This carbon fibre, known to have strong and broadband absorption across the ultraviolet to MIR range, is imaged by the ULM-PAM system with a ultraviolet wavelength of 266 nm and an MIR wavelength of 3,500 nm. For comparison, we also acquired a conventional MIR photoacoustic microscopy (MIR-PAM) image at 3,500 nm wavelength. Figure 2a shows the photoacoustic amplitude profiles across
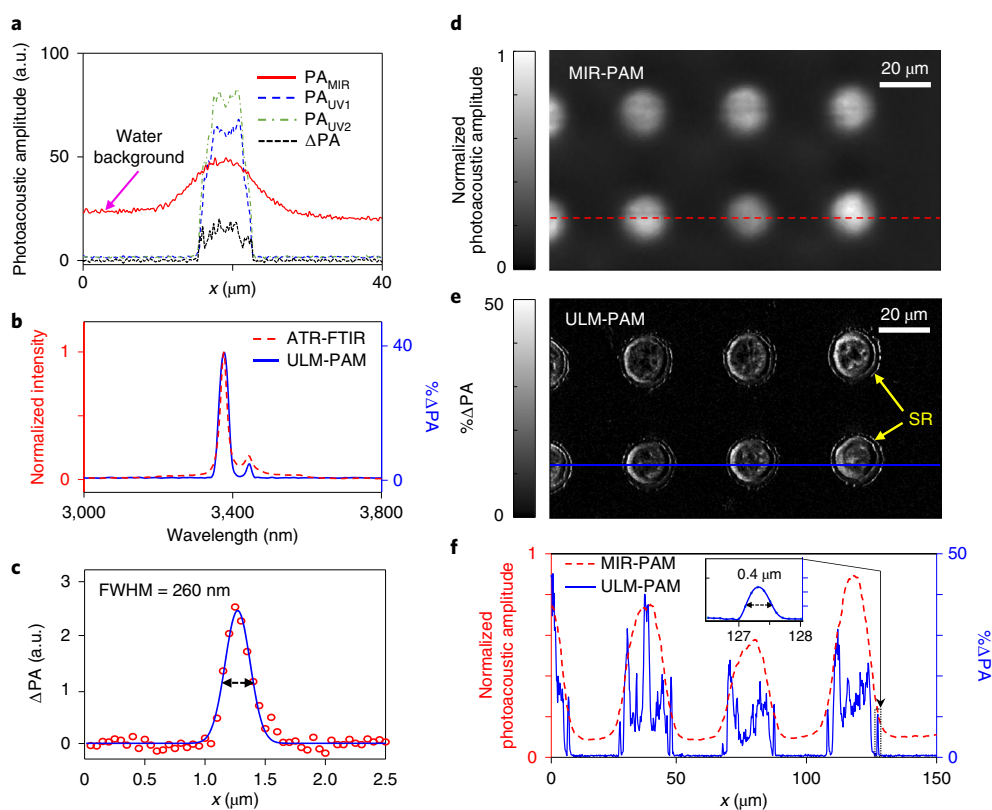
Fig. 2 | System characterization. a, Cross-sectional line images of a 6-μm-diameter carbon fibre. The MIR-PAM image (PA_{MIR}) has a low resolution and a high water background, while the differential image ΔPA has a much sharper edge and lower water background. **b**, Comparison of the ULM-PAM and ATR-FTIR spectra of a thin layer of PDMS. **c**, Effective point spread function of ULM-PAM, measured using a 50-nm-diameter carbon nanobead. **d,e**, Comparison of MIR-PAM (**d**) and ULM-PAM (**e**) images of a VACNT pattern on a MgF$_2$ substrate. SR, satellite rings. **f**, Amplitude profiles along the dashed lines in **d** and **e** showing that MIR-PAM depicts only the envelopes of the VACNT pattern while ULM-PAM shows crisp cross-sectional structures and even 400 nm fine features.

the carbon fibre. The amplitude profile from conventional MIR-PAM (PA_{MIR}) shows a diffraction-limited low spatial resolution and a high water background as the absorption coefficient of water at 3,500 nm is 337.50 cm^{-1} (ref. [48]). In ULM-PAM, by contrast, either the UV-PAM amplitude or ΔPA reveals a much sharper boundary of the fibre with lower water background. However, we use %ΔPA to more directly reveal MIR absorption—that is, to remove the effect of the ultraviolet absorption variation. Note that the maximal %PA is ~25%, corresponding to a temperature rise of 7 °C induced by a single MIR laser pulse. This transient temperature rise has been experimentally shown to be safe to live cells[49].

Second, we verified that ULM-PAM is capable of imaging with MIR vibrational absorption contrast. To this end, we measured a ULM-PAM spectrum (Fig. 2b) of a thin layer (~100 μm) of polydimethylsiloxane (PDMS), which has a sharp methyl group absorption line (CH$_3$) around 3,374 nm (2,964 cm^{-1})[50]. The ULM-PAM spectrum was obtained by averaging 100 measurements to reduce noise and was calibrated according to the pulse energy output of the OPO MIR laser. For verification, we also obtained an MIR spectrum of the same PDMS sample with an ATR-FTIR spectrometer as a ground truth. Figure 2b shows good agreement between the ULM-PAM and ATR-FTIR spectra, validating that ULM-PAM can capture MIR absorption contrast accurately. We focused on the vibrational spectrum of the methyl groups for demonstration, but ULM-PAM can reveal a variety of chemical bonds at MIR wavelengths in principle, whereas pure UV-PAM without MIR mediation[41,47] reflects electronic absorption at ultraviolet wavelengths only.

Third, the spatial resolution of ULM-PAM was quantified to show that MIR imaging with a sub-MIR-diffraction-limited resolution, more than an order of magnitude improvement over conventional MIR imaging resolution, is possible. To this end, we imaged a 50-nm-diameter carbon nanobead in water at 3,500 nm and 224 nm for MIR heating and for ultraviolet probing, respectively. The measured full-width at half-maximum (FWHM) of the single nanobead image from the photoacoustic amplitude profile was 260 nm (Fig. 2c), which is close to the theoretical diffraction-limited resolution (250 nm) achievable with the actual 0.45 NA. In conventional MIR PAM, the theoretical diffraction-limited resolution at 3,500 nm with the same 0.45 NA objective lens is 3,900 nm. One would think single nanobeads may be resolved as long as they are dispersed enough, but their photoacoustic signals are actually overwhelmed by the water background, making them difficult to detect. Because the resolution is determined solely by the ultraviolet focus, we achieved sub-MIR-diffraction-limited MIR imaging with invariant 260 nm ultraviolet resolution.

Fourth, we also demonstrated the resolution of ULM-PAM by imaging patterns of vertically aligned carbon nanotubes (VACNTs) grown onto a MgF$_2$ substrate, which was developed as a broad-spectral resolution target for photoacoustic imaging[51]. As expected, conventional MIR-PAM imaging of the patterns (Fig. 2d) suffers from its large diffraction limit, showing only a broad envelope of the carbon nanotube (CNT) patterns above the water background (Fig. 2f, red dashed line). In comparison, the ULM-PAM image (Fig. 2e) reveals the rich details of the VACNT patterns. Although the VACNTs within the patterns are of the same length, the VACNT density
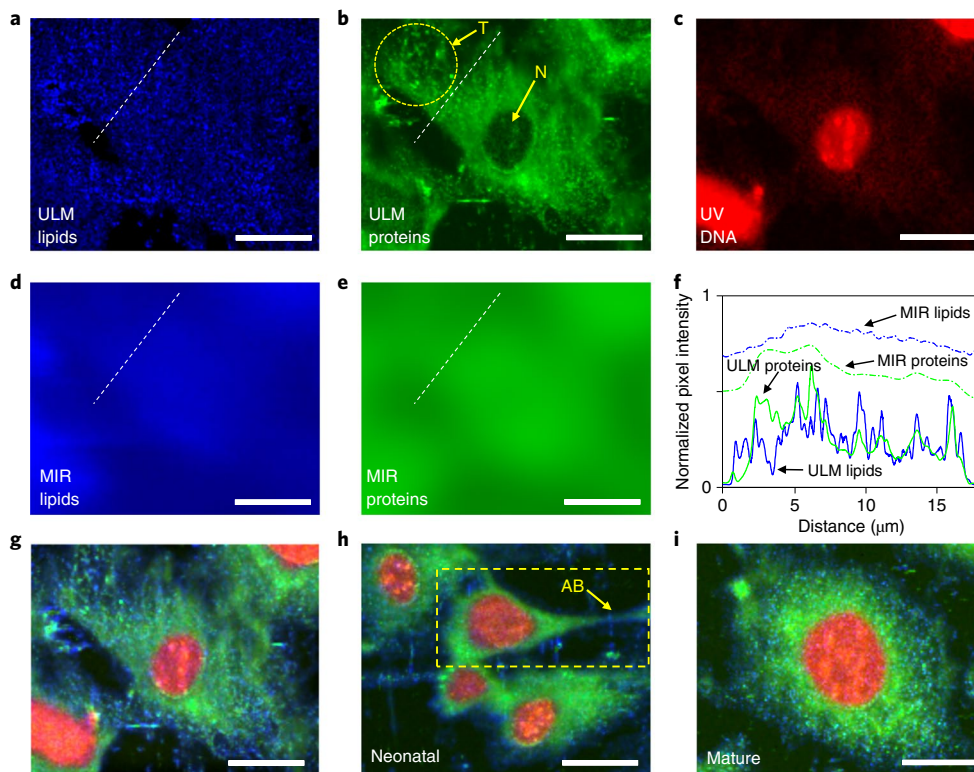
Fig. 3 | Imaging of lipids, proteins and nucleic acids in fibroblast cells. a,b, ULM-PAM images of lipids (**a**) and proteins (**b**). T, tubular structures; N, nucleic region. **c**, UV-PAM image of nucleic acids. **d,e**, MIR-PAM images of lipids (**d**) and proteins (**e**), imaged at 3,420 nm and 6,050 nm, respectively. **f**, Comparison of line profiles along the dashed lines in the ULM-PAM lipid (**a**), ULM-PAM protein (**b**), MIR-PAM lipid (**d**) and MIR-PAM protein (**e**) images. **g**, Composite image of a cell formed by overlaying the images of lipids (**a**), proteins (**b**) and nucleic acids (**c**) in different colour channels. **h,i**, Composite images of the cells at neonatal (**h**) and mature (**i**) stages. AB, actin bundle. Scale bars, 10 µm.

across the pattern may not be uniform due to the non-uniform distribution of growing catalysts during chemical vapour deposition on the MgF$_2$ substrate, and the ULM-PAM in fact reveals photoacoustic amplitude variations within the pattern. Moreover, ULM-PAM detects even finer features, such as satellite rings around the pattern (see image in Fig. 2e, and the amplitude profile across the pattern in Fig. 2f, blue solid line), which may originate from optical lithography artefacts when using a transparent MgF$_2$ substrate with a direct laser writing photography technique (see Supplementary Fig. 2 for confocal backscattered microscopy and transmission optical microscopy images of a VACNT sample from the same batch). The 400 nm FWHM of the satellite rings (inset in Fig. 2f) is comparable to the wavelength of the laser (405 nm) used for direct writing lithography.

To demonstrate the capability of ULM-PAM for subcellular molecular imaging, we prepared freshly formalin-fixed 3T3 mouse fibroblast cells for mapping the distribution of intracellular lipids and proteins. We tuned the ultraviolet wavelength to 224 nm, where almost all proteins, lipids and nucleic acids have strong absorption with molar absorption coefficients on the order of $1 \times 10^4 \, M^{-1} cm^{-1}$ for proteins and $1 \times 10^6 \, M^{-1} cm^{-1}$ for nucleic acids[52]. For lipid imaging, we set the MIR wavelength to the absorption peak at 3,420 nm (2,924 cm^{-1}), corresponding to the asymmetric stretching mode of the CH$_2$ group—the dominant constituent of lipids[6]. The ULM-PAM for lipids resolved many small aggregated globules (Fig. 3a), attributed to rich oleic acid molecules in the droplets. For protein imaging, we used 6,050 nm (1,653 cm^{-1}) to target the amide I band—the most absorptive one in proteins. As shown in Fig. 3b, the signals are scant in the nucleic region and abundant in other regions due to the reduced cytoplasm thickness above, confirming that they are from intracellular organelles. Their tubular or vesicular forms with

gradually decreasing density from the middle to the cell edge indicate that they are protein-containing organelles such as endoplasmic reticulum, Golgi apparatus and secretory vesicles. Furthermore, the filamentous structures near the cell edge are resolved and are probably cytoskeletons in fibroblast cells. MIR microscopy is thus used here to reveal the subcellular protein distribution in hydrated cells at fine resolution. To complete our high-resolution and high-contrast chemical mapping of major intracellular biomolecules, including nucleic acids, we used 250 nm ultraviolet wavelength to directly generate a UV-PAM image (Fig. 3c), based on the strong electronic absorption of nucleic acids[39,47]. The image, with strong signals from the cell nuclei, resolves details of the sub-nucleic distribution of nucleic acids. For this nucleic acid imaging, MIR lasers were not used, because the DNA/RNA is partially invisible in MIR imaging, mainly owing to its band overlap with other chemical bonds and its low MIR absorption[53,54]. The spatial resolution and image contrast stand out when compared with conventional MIR-PAM images of lipids (Fig. 3d) and proteins (Fig. 3e), obtained at 3,420 nm and 6,050 nm, respectively, which display poor spatial resolution and a strong water background. For quantitative assessment, four amplitude profiles across the same line in Fig. 3a,b,d,e are compared in Fig. 3f. The ULM-PAM images reveal many fine features, while the regular MIR-PAM images do not because of the resolution limit. Overlaying the individual images of lipids, proteins and nucleic acids shown in Fig. 3a–c constructs a complete molecular map of a fibroblast cell without labelling (Fig. 3g). This advantage allows us to study cellular metabolisms and activities at different stages. As a demonstration, images of mature (Fig. 3h) and neonatal (Fig. 3i) cells are compared. On the one hand, a broader spatial distribution of proteins and more filamentous structures in the neonatal cells
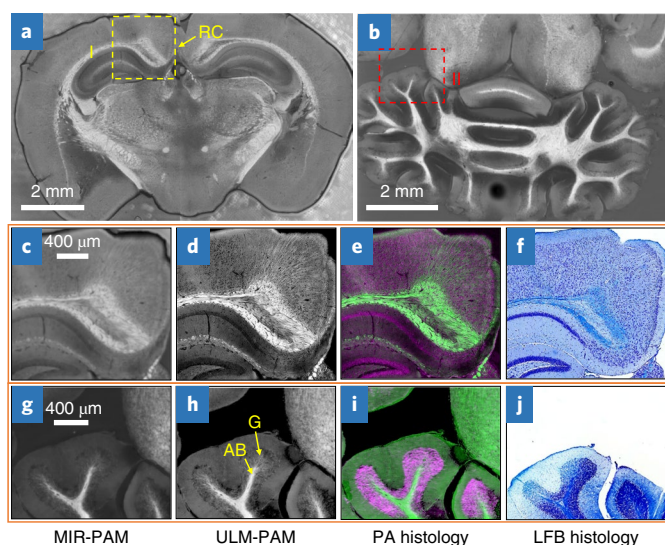
Fig. 4 | Imaging of mouse brain slices. a,b, MIR-PAM images of myelin in 300-µm-thick slices of the cerebrum (**a**) and cerebellum (**b**). RC, retrosplenial cortex. **c**, Close-up MIR-PAM image of myelin. **d**, ULM-PAM image of myelin. **e**, PA histology image. **f**, LFB-stained histology image of the same area (area I) shown in the cerebrum image (**a**). **g**, Close-up MIR-PAM image of myelin. **h**, ULM-PAM image of myelin. AB, arbor vitae region; G, granular region. **i**, Photoacoustic histology image. **j**, LFB-stained histology image of the same area (area II) shown in the cerebellum image (**b**). In the photoacoustic histology images, green represents myelin and violet represents nucleic acids. In the LFB-stained histology images, blue represents myelin and deep blue represents nucleic acids.

imply that the neonatal cells may have more active protein metabolism and higher mobility involving more actin fibres. On the other hand, the mature cell contains more lipid droplets not associated with proteins, indicative of less metabolic activity.

Another important application of ULM-PAM is label-free photoacoustic histology of thick tissue slices. The study of nerve fibres is important in brain science, and myelin is one of the main chemical components of axons in the central nervous system, so we implemented ULM-PAM to study the structural details of the cerebrum and cerebellum in a mouse brain ex vivo. A microtome was used to slice a coronal cerebrum section and a horizontal cerebellum section, both 300 µm thick, from a freshly formalin-fixed mouse brain. Initially, myelin images of these two sections (Fig. 4a,b) in a fully hydrated state were acquired by MIR-PAM at 3,420 nm, which is the peak absorption wavelength of myelin lipids. The MIR-PAM images of the cerebrum and cerebellum sections are both similar to histology or dye-stained fluorescence images, exhibiting rich structural information about the nerve fibres or fibre bundles. However, in low spatial resolution and low contrast MIR-PAM images, finer details such as concentration gradient and structural details across the boundary between the retrosplenial cortex and grey cortical region are hardly resolved.

To reveal the finer details, we used ULM-PAM, with an ultraviolet wavelength of 224 nm and an MIR wavelength of 3,420 nm, to achieve higher-resolution and water-background-free MIR imaging of the myelin in the tissue. We first used MIR-PAM to scan a small area of interest (Fig. 4c), which corresponds to the retrosplenial cortex in the cerebrum (region I in Fig. 4a), and then used ULM-PAM to image the same area (Fig. 4d) for comparison. The ULM-PAM clearly resolves fine structures of nerve fibres or bundles in the retrosplenial cortical region. We further overlaid the ULM-PAM image of myelin with an UV-PAM image of nucleic acids acquired at 250 nm (Supplementary Fig. 3), yielding a histology-like image

(Fig. 4e). We call this method 'photoacoustic histology', showing both myelin (green) and nucleic acid (purple) distributions. To validate the photoacoustic histology image, the same brain slice was further sectioned into thinner slices, stained by myelin axon-specific Luxol fast blue (LFB), and imaged by conventional optical microscopy (Fig. 4f). The photoacoustic histology image (Fig. 4e) and the LFB-stained image (Fig. 4f) show the same details, with concentrated myelin distributions in the RC (bright green in the photoacoustic histology and bright blue in the LFB stain histology) and punctate pattern indicative of cell nuclei (purple in the photoacoustic histology and punctate dark blue in the LFB stain histology). In addition, we performed the same experiment on another region (region II in Fig. 4b) of the cerebellum section. The resulting ULM-PAM image (Fig. 4h) shows dense nerve bundles in the arbor vitae region and sparse but clear nerve fibres radiating into the granular region, whereas the photoacoustic histology image (Fig. 4i) reveals the densely distributed nucleic acids of non-myelinated cells in the granular region. The LFB-stained image (Fig. 4j) also validates the photoacoustic histology image of region II in the cerebellum section. These results demonstrate that ULM-PAM is capable of imaging the myelin distribution and revealing nerve fibres or bundles in thick brain slices at high resolution and low water background without any exogenous labels. Furthermore, aided by UV-PAM imaging of nucleic acids, it can generate photoacoustic histology images that are similar to standard LFB-stained histology images.

Discussion

ULM-PAM is a novel high-resolution and water-background-suppressed MIR microscopy modality capable of imaging fresh biological samples without staining. For cells, ULM-PAM provides subcellular MIR imaging of lipids and proteins with high contrast without the highly obscuring water background. For tissue slices, ULM-PAM produces label-free photoacoustic histology images without requiring thin slicing and drying of samples, unlike conventional MIR imaging[6]. At the MIR wavelength of 3,420 nm—targeting CH_2 stretching—water absorbs less than the molecules of interest, and at the ultraviolet wavelength water is almost transparent. Accordingly, ULM-PAM eliminates the water background nearly completely. At the MIR wavelengths where water absorbs more than the molecules of interest, for example, the amide A band around 3,000 nm, neighbouring water within the thermal diffusion range may interfere with the temperature rise of the targeted molecules. However, by shortening the time delay between the MIR and ultraviolet pulses[55], the thermal diffusion length can be reduced to <50 nm, far less than the ultraviolet focal diameter. Consequently, the effect of neighbouring water is substantially suppressed. Our initial system can be extended to cover the full MIR spectral range, allowing exploration of many more molecules of interest. To our knowledge, among the existing far-field MIR imaging approaches, ULM-PAM has achieved the highest imaging resolution at 250 nm, which can be further improved by using a higher-NA objective lens and a shorter ultraviolet wavelength. In addition, ULM-PAM can potentially bridge the resolution gap from 100 nm to 400 nm between AFM-MIR and other MIR imaging modalities, such as ATR-FTIR and photothermal MIR.

Currently, ULM-PAM still faces some technical limitations. First, although raw photoacoustic amplitudes have high signal-to-noise ratios, their fractional changes are noisy, mainly because two successive ultraviolet laser pulses are non-identical. Our current ultraviolet laser has ~25% energy fluctuation at 224 nm with additional mode hopping, which cannot be easily compensated by photodiode calibration. A more stable ultraviolet laser would greatly benefit ULM-PAM. Alternatively, a long optical-fibre delay line could be used to replicate the ultraviolet pulse with a preset time delay to avoid inter-pulse fluctuation. In addition, the pulse energy of our current MIR laser in the fingerprint region (>6,600 nm)

fluctuates so prominently that ULM-PAM could not be realized stably. Second, the imaging speed is restricted by the pulse repetition rates of the lasers, currently only up to 1 kHz, which is inadequate for real-time imaging. For example, it takes more than 2 h to scan a 1 mm × 1 mm area with a 500 nm step size, and usually more than ten scans are needed for averaging, to compensate for the inter-pulse fluctuation. If the pulse repetition rate reaches 200 kHz and the pulse energy is sufficiently stable, the imaging time without averaging can be reduced by 200 times to about 40 s. Furthermore, multifocal photoacoustic imaging using a linear array of ultrasonic transducers can improve the imaging speed dramatically, typically more than 100 times[56,57]. In this way, the acquisition time can potentially be shortened to 0.4 s, enabling in vivo imaging. ULM-PAM can also explore the fingerprint region to yield rich vibration information. Third, our current transmission-mode system cannot be switched to reflection mode because an MIR-transparent coupling medium with low acoustic attenuation has not been found. To realize the reflection mode, surface-wave acoustic detection may be employed. Fourth, depth cannot be optically resolved in the current system. Because the focal zone of the MIR laser is much longer than that of the ultraviolet laser, the axial resolution is the same as that of conventional UV-PAM, which lacks optical sectioning capability. A cross-beam configuration, in which the MIR and ultraviolet laser beams cross at an angle while confocally targeting the same object, may improve the axial resolution.

Thus far, two vibrational imaging microscopies provide far-field and label-free imaging at subcellular resolution: Raman scattering microscopy[58,59] and photothermal MIR microscopy[21,23]. First, compared with Raman scattering microscopy, ULM-PAM—leveraging direct MIR photon absorption—is of higher sensitivity, because the fundamental MIR cross-section is several orders of magnitude greater than the Raman scattering cross-section[7]. Second, ULM-PAM not only exhibits the same features as Raman scattering microscopy, such as low water background, but can also be extended to direct imaging of various vibrational bonds that are not Raman-active in the wide mid-MIR spectral range[23]. Third, ULM-PAM provides a higher spatial resolution due to the short ultraviolet wavelength. Compared with photothermal MIR microscopy, our method is essentially a new way to exploit the MIR photothermal effect, but we use photoacoustic detection instead to retrieve the MIR-absorption-induced local temperature rise, enabling MIR imaging in thick, highly optically absorbing and scattering biological samples. More importantly, photoacoustic temperature sensing is based on the Grüneisen relaxation effect, which gives a photoacoustic signal change of about 3% per °C in the physiological temperature range. This change is two orders of magnitude greater than the photothermally induced refractive index change (~10^{-4} per °C), making ULM-PAM more sensitive than photothermal MIR microscopy. In this work, ULM-PAM imaged a 50 nm bead in water (Fig. 2c) with a signal-to-noise ratio of about 7, while the total data acquisition time was only about 1 μs for each pixel, outperforming the current photothermal MIR microscopy based on lock-in detection[23,24]. Furthermore, because water is almost transparent at ultraviolet wavelengths from 200 to 230 nm, the water background of MIR imaging is suppressed in ULM-PAM. Finally, the shorter ultraviolet wavelength endows our method with higher resolution than photothermal MIR imaging, which is based on visible or near-infrared light detection.

Our method can be further developed to attain nanoscale far-field chemical imaging by extending the wavelength of the probe beam to the X-ray regime. Current X-ray microscopy for biological samples operates either in the soft X-ray regime for water transparency (2.33–4.40 nm) or the hard X-ray regime[60,61], using imaging contrast arising from natural X-ray absorption to provide nanometre-scale resolution. Imaging specific chemicals or structures inside biological samples requires exogenous labelling, for example,

silver-enhanced immunogold labelling[62]. Interestingly, X-ray acoustic imaging has also been demonstrated with a pulsed X-ray source[63]. By combining the MIR-absorption induced Grüneisen relaxation effect and X-ray-acoustic imaging, we can expect to achieve X-ray-acoustic imaging with MIR-absorption contrast, utilizing acoustic signals generated by pulsed X-rays to report MIR absorption contrast in materials, thereby achieving far-field and label-free imaging at nanometre-scale resolution.

Online content

Any methods, additional references, Nature Research reporting summaries, source data, statements of code and data availability and associated accession codes are available at https://doi.org/10.1038/s41566-019-0441-3.

References

1. Wetzel, D. L. & LeVine, S. M. Imaging molecular chemistry with infrared microscopy. *Science* **285**, 1224–1225 (1999).
2. Koenig, J. L. *Microspectroscopic Imaging of Polymers* (American Chemical Society, 1998).
3. Prati, S., Joseph, E., Sciutto, G. & Mazzeo, R. New advances in the application of FTIR microscopy and spectroscopy for the characterization of artistic materials. *Acc. Chem. Res.* **43**, 792–801 (2010).
4. Diem, M., Romeo, M., Boydston-White, S., Miljkovic, M. & Matthaus, C. A decade of vibrational micro-spectroscopy of human cells and tissue (1994–2004). *Analyst* **129**, 880–885 (2004).
5. Fernandez, D. C., Bhargava, R., Hewitt, S. M. & Levin, I. W. Infrared spectroscopic imaging for histopathologic recognition. *Nat. Biotechnol.* **23**, 469–474 (2005).
6. Baker, M. J. et al. Using Fourier transform IR spectroscopy to analyze biological materials. *Nat. Protoc.* **9**, 1771–1791 (2014).
7. Diem, M. et al. Molecular pathology via IR and Raman spectral imaging. *J. Biophoton.* **6**, 855–886 (2013).
8. Griffiths, P. Fourier transform infrared spectrometry. *Science* **21**, 297–302 (1983).
9. Lewis, E. N. et al. Fourier transform spectroscopic imaging using an infrared focal-plane array detector. *Anal. Chem.* **67**, 3377–3381 (1995).
10. Miller, L. M., Smith, G. D. & Carr, G. L. Synchrotron-based biological microspectroscopy: from the mid-infrared through the far-infrared regimes. *J. Biol. Phys.* **29**, 219–230 (2003).
11. Nasse, M. J. et al. High-resolution Fourier-transform infrared chemical imaging with multiple synchrotron beams. *Nat. Methods* **8**, 413–416 (2011).
12. Kole, M. R., Reddy, R. K., Schulmerich, M. V., Gelber, M. K. & Bhargava, R. Discrete frequency infrared microspectroscopy and imaging with a tunable quantum cascade laser. *Anal. Chem.* **84**, 10366–10372 (2012).
13. Haas, J. & Mizaikoff, B. Advances in mid-infrared spectroscopy for chemical analysis. *Annu. Rev. Anal. Chem.* **9**, 45–68 (2016).
14. Sommer, A. J., Marcott, C., Story, G. M. & Tisinger, L. G. Attenuated total internal reflection infrared mapping microspectroscopy using an imaging microscope. *Appl. Spectrosc.* **55**, 252–256 (2001).
15. Chan, K. L. A. & Kazarian, S. G. New opportunities in micro- and macro-attenuated total reflection infrared spectroscopic imaging: spatial resolution and sampling versatility. *Appl. Spectrosc.* **57**, 381–389 (2003).
16. Dazzi, A., Prazeres, R., Glotin, F. & Ortega, J. M. Local infrared microspectroscopy with subwavelength spatial resolution with an atomic force microscope tip used as a photothermal sensor. *Opt. Lett.* **30**, 2388–2390 (2005).
17. Lu, F., Jin, M. & Belkin, M. A. Tip-enhanced infrared nanospectroscopy via molecular expansion force detection. *Nat. Photon.* **8**, 307–312 (2014).
18. Dazzi, A. & Prater, C. B. AFM-IR: technology and applications in nanoscale infrared spectroscopy and chemical imaging. *Chem. Rev.* **117**, 5146–5173 (2017).
19. Knoll, B. & Keilmann, F. Near-field probing of vibrational absorption for chemical microscopy. *Nature* **399**, 134–137 (1999).
20. Nowak, D. et al. Nanoscale chemical imaging by photoinduced force microscopy. *Sci. Adv.* **2**, e1501571 (2016).
21. Furstenberg, R., Kendziora, C. A., Papantonakis, M. R., Nguyen, V. & McGill, R. A. Chemical imaging using infrared photothermal microspectroscopy. In *Proceedings of SPIE Defense, Security, and Sensing* (eds Druy, M. A. & Crocombe, R. A.) 837411 (SPIE, 2012).
22. Li, Z., Kuno, M. & Hartland, G. Super-resolution imaging with mid-IR photothermal microscopy on the single particle level. In *Proceedings of SPIE Physical Chemistry of Interfaces and Nano-materials XIV* (eds Hayes, S. C. & Bittner, E. R.) 954912 (International Society for Optics and Photonics, 2015).

23. Zhang, D. et al. Depth-resolved mid-infrared photothermal imaging of living cells and organisms with submicrometer spatial resolution. *Sci. Adv.* **2**, e1600521 (2016).
24. Li, Z., Aleshire, K., Kuno, M. & Hartland, G. V. Super-resolution far-field infrared imaging by photothermal heterodyne imaging. *J. Phys. Chem. B* **121**, 8838–8846 (2017).
25. Lu, F.-K. et al. Label-free DNA imaging in vivo with stimulated Raman scattering microscopy. *Proc. Natl Acad. Sci. USA* **112**, 11624–11629 (2015).
26. Cheng, J.-X. & Xie, X. S. Vibrational spectroscopic imaging of living systems: an emerging platform for biology and medicine. *Science* **350**, aaa8870 (2015).
27. Ji, M. et al. Detection of human brain tumor infiltration with quantitative stimulated Raman scattering microscopy. *Sci. Transl. Med.* **7**, 309ra163 (2015).
28. Gong, L. & Wang, H. Breaking the diffraction limit by saturation in stimulated-Raman-scattering microscopy: a theoretical study. *Phys. Rev. A* **90**, 13818 (2014).
29. Ruchira Silva, W., Graefa, C. T. & Frontiera, R. R. Toward label-free super-resolution microscopy. *ACS Photon.* **3**, 79–86 (2016).
30. Rockley, M. G. Fourier-transformed infrared photoacoustic spectroscopy of polystyrene film. *Chem. Phys. Lett.* **68**, 455–456 (1979).
31. Patel, C. K. N. & Tam, A. C. Pulsed optoacoustic spectroscopy of condensed matter. *Rev. Mod. Phys.* **53**, 517–550 (1981).
32. Tam, A. C. Applications of photoacoustic sensing techniques. *Rev. Mod. Phys.* **58**, 381–431 (1986).
33. Michaelian, K. H. *Photoacoustic Infrared Spectroscopy* (Wiley, 2003).
34. Sim, J. Y., Ahn, C.-G., Jeong, E.-J. & Kim, B. K. In vivo microscopic photoacoustic spectroscopy for non-invasive glucose monitoring invulnerable to skin secretion products. *Sci. Rep.* **8**, 1059 (2018).
35. Wang, L., Zhang, C. & Wang, L. V. Grueneisen relaxation photoacoustic microscopy. *Phys. Rev. Lett.* **113**, 174301 (2014).
36. Lai, P., Wang, L., Tay, J. W. & Wang, L. V. Photoacoustically guided wavefront shaping for enhanced optical focusing in scattering media. *Nat. Photon.* **9**, 126–132 (2015).
37. Kunitz, M. Crystalline desoxyribonuclease; isolation and general properties; spectrophotometric method for the measurement of desoxyribonuclease activity. *J. Gen. Physiol.* **33**, 349–362 (1950).
38. Beaven, G. H. & Holiday, E. R. Ultraviolet absorption spectra of proteins and amino acids. *Adv. Protein Chem* **7**, 319–386 (1952).
39. Yao, D.-K., Maslov, K. I., Wang, L. V., Chen, R. & Zhou, Q. Optimal ultraviolet wavelength for in vivo photoacoustic imaging of cell nuclei. *J. Biomed. Opt.* **17**, 056004 (2012).
40. Quickenden, T. I. & Irvin, J. A. The ultraviolet absorption spectrum of liquid water. *J. Chem. Phys.* **72**, 4416–4428 (1980).
41. Wong, T. T. W. et al. Fast label-free multilayered histology-like imaging of human breast cancer by photoacoustic microscopy. *Sci. Adv.* **3**, e1602168 (2017).
42. Danielli, A. et al. Label-free photoacoustic nanoscopy. *J. Biomed. Opt.* **19**, 086006 (2014).
43. Xu, S., Scherer, G. W., Mahadevan, T. S. & Garofalini, S. H. Thermal expansion of confined water. *Langmuir* **25**, 5076–5083 (2009).
44. Larina, I. V., Larin, K. V. & Esenaliev, R. O. Real-time optoacoustic monitoring of temperature in tissues. *J. Phys. D* **38**, 2633–2639 (2005).
45. Shah, J. et al. Photoacoustic imaging and temperature measurement for photothermal cancer therapy. *J. Biomed. Opt.* **13**, 034024 (2008).
46. Yao, J., Ke, H., Tai, S., Zhou, Y. & Wang, L. V. Absolute photoacoustic thermometry in deep tissue. *Opt. Lett.* **38**, 5228–5231 (2013).
47. Yao, D.-K., Maslov, K., Shung, K. K., Zhou, Q. & Wang, L. V. In vivo label-free photoacoustic microscopy of cell nuclei by excitation of DNA and RNA. *Opt. Lett.* **35**, 4139–4141 (2010).
48. Hale, G. M. & Querry, M. R. Optical constants of water in the 200-nm to 200-μm wavelength region. *Appl. Opt.* **12**, 555–563 (1973).
49. Simanovskii, D. M. et al. Cellular tolerance to pulsed hyperthermia. *Phys. Rev. E* **74**, 011915 (2006).
50. Mata, A., Fleischman, A. J. & Roy, S. Characterization of polydimethylsiloxane (PDMS) properties for biomedical micro/nanosystems. *Biomed. Microdev.* **7**, 281–293 (2005).
51. Hwang, J. et al. Development of photoacoustic phantoms towards quantitative evaluation of photoacoustic imaging devices. In *SPIE Photonics West* 10494–77 (SPIE, 2018).
52. Schmid, F.-X. Biological macromolecules: UV-visible spectrophotometry in *Encyclopedia of Life Sciences* (Macmillan Publishers Ltd, Nature Publishing Group, 2001).
53. Lasch, P., Boese, M., Pacifico, A. & Diem, M. FT-IR spectroscopic investigations of single cells on the subcellular level. *Vibr. Spectrosc.* **28**, 147–157 (2002).
54. Wood, B. R. The importance of hydration and DNA conformation in interpreting infrared spectra of cells and tissues. *Chem. Soc. Rev.* **45**, 1980–1998 (2016).
55. Wang, L. V. & Wu, H. *Biomedical Optics: Principles and Imaging* (Wiley-Interscience, 2007).
56. Song, L., Maslov, K. & Wang, L. V. Multifocal optical-resolution photoacoustic microscopy in vivo. *Opt. Lett.* **36**, 1236–1238 (2011).
57. Imai, T. et al. High-throughput ultraviolet photoacoustic microscopy with multifocal excitation. *J. Biomed. Opt.* **23**, 036007 (2018).
58. Evans, C. L. & Xie, X. S. Coherent anti-Stokes Raman scattering microscopy: chemical imaging for biology and medicine. *Annu. Rev. Anal. Chem.* **1**, 883–909 (2008).
59. Zhang, C., Zhang, D. & Cheng, J.-X. Coherent Raman scattering microscopy in biology and medicine. *Annu. Rev. Biomed. Eng.* **17**, 415–445 (2015).
60. Sakdinawat, A. & Attwood, D. Nanoscale X-ray imaging. *Nat. Photon.* **4**, 840–848 (2010).
61. Berglund, M., Rymell, L., Peuker, M., Wilhein, T. & Hertz, H. M. Compact water-window transmission X-ray microscopy. *J. Microsc.* **197**, 268–273 (2000).
62. Meyer-Ilse, W. et al. High resolution protein localization using soft X-ray microscopy. *J. Microsc.* **201**, 395–403 (2001).
63. Xiang, L., Tang, S., Ahmad, M. & Xing, L. High resolution X-ray-induced acoustic tomography. *Sci. Rep.* **6**, 26118 (2016).

Author contributions

J.S., K.M. and L.V.W. designed the experiment. J.S., T.T.W.W., Y.H. and R.Z. contributed to the system construction. J.S. and T.T.W.W. prepared the brain slices. Y.H. prepared the cell culture. C.S.Y. and J.H. designed and prepared the CNT pattern on a MgF2 substrate. L.L. helped with LFB staining. J.S., K.M., T.T.W.W., Y.H. and L.L. were involved in discussions. J.S. performed the experiment and data analysis. L.V.W supervised the project. All authors were involved in manuscript preparation.

Competing interests

L.V.W. and K.M. have financial interests in Microphotoacoustics, Inc., CalPACT, LLC and Union Photoacoustic Technologies, Ltd, which did not support this work.

Additional information

Supplementary information is available for this paper at https://doi.org/10.1038/s41566-019-0441-3.

Reprints and permissions information is available at www.nature.com/reprints.

Correspondence and requests for materials should be addressed to L.V.W.

Publisher's note: Springer Nature remains neutral with regard to jurisdictional claims in published maps and institutional affiliations.

Methods

System configuration. We used an OPO mid-MIR laser (NT242-SH, EKSPLA) and an OPO ultraviolet laser (NT270, EKSPLA). The wavelength of the OPO mid-MIR laser is tunable from 2.5 to 12 μm (from 4,000 to 833 cm^{-1}), its pulse duration is about 10 ns, and the output pulse energy varies from 10 to 100 μJ depending on the selected wavelength. Both lasers have a pulse repetition rate of up to 1 kHz. The two lasers were synchronized with external triggers, controlling the delay between the ultraviolet and MIR laser pulses. For imaging lipids and proteins using ULM-PAM, the ultraviolet laser was tuned to 224 nm; for imaging nucleic acids using UV-PAM, it was set to 250 nm. Both the MIR and ultraviolet beams, with diameters of about 4 mm, were reflected by several ultraviolet-enhanced aluminium-coated mirrors (PF10-03-F01, Thorlabs) and focused to a sample mounted on a CaF$_2$ window through a ×36 reflective objective lens (50102-02, Newport, 0.52 NA). Photoacoustic signals were detected in transmission mode by a focused ultrasonic transducer (25 MHz centre frequency, V324-SM, Olympus) with an acoustic focal length of 12.7 mm and an element diameter of 6 mm. The acoustic coupling medium was de-ionized water. Photoacoustic signals were amplified by ~50 dB using two low-noise amplifiers (ZFL-500LN+, Mini-circuits) and then acquired by a DAQ card (Razor 14, Gage) at 14 bits and 200 MS s^{-1}.

Raster scanning for images. ULM-PAM images of the sample at selected wavelengths were obtained by raster scanning using two motorized stages (PLS-85, PI miCos) coupled to the sample holder. To drive the scanning stages at high precision (50 nm step size) with minimal low-frequency vibration, we used two five-phase stepper motors (PKP546MN18B, Oriental Motor) and their associated drivers (CVD518-K, Oriental Motor). Line scans along the *x* axis were averaged to compensate for ultraviolet laser inter-pulse fluctuation. The laser tuning, data acquisition and scanning systems were synchronized by a central computer via microcontrollers, using LabVIEW. The scan step size varied for different samples. The point spread function of a 50-nm-diameter carbon nanobead was measured using a step size of 50 nm. Imaging of cells was carried out with a step size of 200 nm. For imaging of brain slices, to compensate for the slow laser repetition rates of the lasers, we shrank the ultraviolet beam to reduce the effective NA to 0.16, which worsened the resolution to some extent, but accelerated the scanning with a larger step size (500 nm) and effectively extended the focal depth to accommodate uneven sample surfaces.

ATR-FTIR measurements. All ATR-FTIR spectra were measured on an ATR-FTIR spectrometer (Nicolet 6700, Thermo) in the Molecular Materials Research Center at California Institute of Technology. The baseline was calibrated by measuring a blank sample.

For the spatial resolution measurement, carbon nanoparticles (~50 nm diameter; US1074, US Research Nanomaterials) were sparsely distributed on the surface of a CaF$_2$ window. A layer of low-gelling-temperature agarose (A9414-100G, Sigma-Aldrich) was placed on top of the window to fix the nanoparticles. The sample was imaged in 50 nm steps.

Cell culture preparation. Mouse embryonic fibroblast cells (3T3-L1) were obtained from the American Type Culture Collection (ATCC). The cells were seeded onto 1-mm-thick CaF$_2$ substrates, and then maintained at 37 °C and 5% CO$_2$ in Dulbecco's modified Eagle's medium (DMEM, Sigma Aldrich) supplemented with 10% bovine calf serum (Sigma Aldrich). When the cells were ~100% confluent, to induce some cells to form oleic acid droplets, the medium was changed to adipocyte differentiation medium containing 90% DMEM, 10% fetal bovine serum, 1.0 μM dexamethasone, 0.5 mM isobutylmethylxanthine and 1.0 μg ml^{-1} insulin, all from Sigma Aldrich. Two days later, the medium was changed to adipocyte maintenance medium (90% DMEM, 10% fetal bovine serum and 1.0 μg ml^{-1} insulin), and incubated for another two days. Finally, partially differentiated cells were fixed in 3.7% formalin solution, and washed with phosphate buffered saline.

Tissue slice preparation. The brain was extracted from Swiss Webster mice (Hsd: ND4, Harlan Laboratories) and fixed in 3.7% formalin solution at room temperature. Afterwards, the fixed brain was embedded in 4% agarose and then sectioned by a microtome (VT1200S, Leica) into slices (300 μm thick). All experimental animal procedures were carried out in conformity with a laboratory animal protocol approved by the Animal Studies Committee of California Institute of Technology. After they were imaged by ULM-PAM, the thick slices underwent standard procedures for histological staining (including paraffinization, slicing (10 μm thickness) and staining), and were finally imaged in a digital pathology system (VENTANA iScan HT, Roche). It should be noted that some samples were fragmented and slightly distorted during the thin-slicing procedure, which did not affect the comparison. The LFB-stained histology images of the cerebrum and cerebellum are shown in Supplementary Fig. 4.

Data analysis. Raw photoacoustic data for each pixel were acquired within a time window of 0.5 μs for one laser shot. For calibration, each ultraviolet photoacoustic signal was divided by the maximal value of the photodiode signal pulse by pulse. Photoacoustic signals were bandpass-filtered to remove noise outside the transducer's bandwidth. The difference signal $\Delta PA = PA_{UV2} - PA_{UV1}$ was calculated in the time domain, and its maximum amplitude projection was computed to construct an image. The fractional change in photoacoustic amplitude was computed by $\%\Delta PA = \Delta PA/(PA_{UV1} + \lambda)$, where λ was chosen as several times the root-mean-square noise level. This technique is similar to the Tikhonov regularization. The final images were further processed with a median filter to reduce salt-and-pepper noise.

Reporting Summary. Further information on research design is available in the Nature Research Reporting Summary linked to this article.

Data availability

The data that support the plots within this paper and other findings of this study are available from the corresponding author upon reasonable request.

Code availability

The code that supports the plots within this paper and other findings of this study are available from the corresponding author upon reasonable request.

nature research

Corresponding author(s):	Lihong Wang
Last updated by author(s):	Apr 8, 2019

Reporting Summary

Nature Research wishes to improve the reproducibility of the work that we publish. This form provides structure for consistency and transparency in reporting. For further information on Nature Research policies, see Authors & Referees and the Editorial Policy Checklist.

Statistics

For all statistical analyses, confirm that the following items are present in the figure legend, table legend, main text, or Methods section.

n/a	Confirmed	
☒	☐	The exact sample size (n) for each experimental group/condition, given as a discrete number and unit of measurement
☒	☐	A statement on whether measurements were taken from distinct samples or whether the same sample was measured repeatedly
☒	☐	The statistical test(s) used AND whether they are one- or two-sided *Only common tests should be described solely by name; describe more complex techniques in the Methods section.*
☒	☐	A description of all covariates tested
☒	☐	A description of any assumptions or corrections, such as tests of normality and adjustment for multiple comparisons
☒	☐	A full description of the statistical parameters including central tendency (e.g. means) or other basic estimates (e.g. regression coefficient) AND variation (e.g. standard deviation) or associated estimates of uncertainty (e.g. confidence intervals)
☒	☐	For null hypothesis testing, the test statistic (e.g. F, t, r) with confidence intervals, effect sizes, degrees of freedom and P value noted *Give P values as exact values whenever suitable.*
☒	☐	For Bayesian analysis, information on the choice of priors and Markov chain Monte Carlo settings
☒	☐	For hierarchical and complex designs, identification of the appropriate level for tests and full reporting of outcomes
☒	☐	Estimates of effect sizes (e.g. Cohen's d, Pearson's r), indicating how they were calculated

Our web collection on statistics for biologists contains articles on many of the points above.

Software and code

Policy information about availability of computer code

Data collection	LabVIEW 2015, AlazarTech ATS-VI 5.8.3
Data analysis	Matlab 2016a

For manuscripts utilizing custom algorithms or software that are central to the research but not yet described in published literature, software must be made available to editors/reviewers. We strongly encourage code deposition in a community repository (e.g. GitHub). See the Nature Research guidelines for submitting code & software for further information.

Data

Policy information about availability of data

All manuscripts must include a data availability statement. This statement should provide the following information, where applicable:
- Accession codes, unique identifiers, or web links for publicly available datasets
- A list of figures that have associated raw data
- A description of any restrictions on data availability

The data and code that support the plots within this paper and other findings of this study are available from the corresponding author upon reasonable request.

Field-specific reporting

Please select the one below that is the best fit for your research. If you are not sure, read the appropriate sections before making your selection.

☒ Life sciences   ☐ Behavioural & social sciences   ☐ Ecological, evolutionary & environmental sciences

For a reference copy of the document with all sections, see nature.com/documents/nr-reporting-summary-flat.pdf

Life sciences study design

All studies must disclose on these points even when the disclosure is negative.

Sample size	Three batches of cell cultures and two mouse brain samples were used to repeat the experiment. No statistical analysis is required for the report of our method rather than for specific and comprehensive biological studies.
Data exclusions	More cell images were not shown in this work. We exhibited some typically images of cells that shows the advantages of our reported method.
Replication	The cell culture imaging was repeated by three times and mouse brain imaging was repeated by two times.
Randomization	The samples were not randomized. The cells and mouse brain slices were included to demonstrate the unique capabilities of ULM-PAM rather than for specific and comprehensive biological studies.
Blinding	Investigators were not blinded to group allocation.

Reporting for specific materials, systems and methods

We require information from authors about some types of materials, experimental systems and methods used in many studies. Here, indicate whether each material, system or method listed is relevant to your study. If you are not sure if a list item applies to your research, read the appropriate section before selecting a response.

Materials & experimental systems

n/a	Involved in the study
☒	☐ Antibodies
☐	☒ Eukaryotic cell lines
☒	☐ Palaeontology
☐	☒ Animals and other organisms
☒	☐ Human research participants
☒	☐ Clinical data

Methods

n/a	Involved in the study
☒	☐ ChIP-seq
☒	☐ Flow cytometry
☒	☐ MRI-based neuroimaging

Eukaryotic cell lines

Policy information about cell lines

Cell line source(s)	The 3T3-L1 mouse embryonic fibroblast cell line.
Authentication	The 3T3-L1 cell line used was authenticated by American Type Culture Collection (ATCC) before it was delivered to us.
Mycoplasma contamination	The 3T3-L1 cell line was tested for mycoplasma contamination by American Type Culture Collection (ATCC).
Commonly misidentified lines (See ICLAC register)	No commonly misidentified cell lines were used.

Animals and other organisms

Policy information about studies involving animals; ARRIVE guidelines recommended for reporting animal research

Laboratory animals	The brain was extracted from the Swiss Webster mice (Hsd: ND4, Harlan Laboratories)
Wild animals	No wild animals were used.
Field-collected samples	No sample was collected from the field for this study.
Ethics oversight	All experimental animal procedures were carried out in conformity with a laboratory animal protocol approved by the Animal Studies Committee of California Institute of Technology.

Note that full information on the approval of the study protocol must also be provided in the manuscript.